Accepted Manuscript

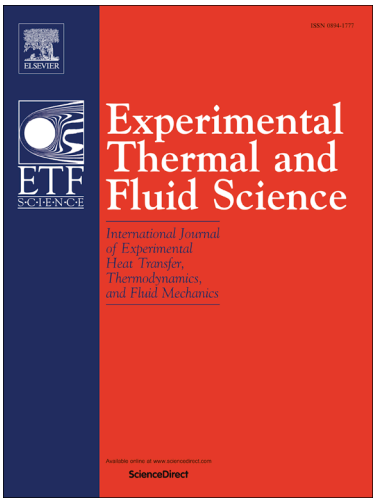

Combined particle image velocimetry / digital image correlation for load estimation

Peng Zhang, Sean D. Peterson, Maurizio Porfiri

PII: S0894-1777(18)31118-X
DOI: https://doi.org/10.1016/j.expthermflusci.2018.09.011
Reference: ETF 9607

To appear in: *Experimental Thermal and Fluid Science*

Received Date: 18 June 2018
Accepted Date: 11 September 2018

Please cite this article as: P. Zhang, S.D. Peterson, M. Porfiri, Combined particle image velocimetry / digital image correlation for load estimation, *Experimental Thermal and Fluid Science* (2018), doi: https://doi.org/10.1016/j.expthermflusci.2018.09.011

Combined particle image velocimetry / digital image correlation for load estimation

Peng Zhang[a], Sean D. Peterson[a,b], Maurizio Porfiri[a,*]

[a] *Department of Mechanical and Aerospace Engineering, New York University Tandon School of Engineering, Six MetroTech Center, Brooklyn, NY 11201, USA*

[b] *Department of Mechanical and Mechatronics Engineering, University of Waterloo, 200 University Avenue West, Waterloo, ON N2L 3G1, Canada*

Abstract

Particle image velocimetry (PIV) and digital image correlation (DIC) are widely used experimental techniques in fluid mechanics and structural dynamics, respectively. PIV is capable of resolving detailed velocity fields around structures, from which the hydrodynamic loading can be reconstructed. However, PIV is ill-suited to capturing the structural response, which is critical for a complete understanding of the bidirectional coupling between the fluid flow and the structural dynamics. On the other hand, DIC can accurately quantify local deformation of the structure, but does not afford the precise identification of the hydrodynamic loading due to the ill-posed nature of the inverse load estimation process. Here, we explore the feasibility of a combined PIV/DIC technique for the investigation of fluid-structure interactions. Specifically, we study fluid-structure interactions associated with a flexible cantilever plate immersed in a steady unidirectional flow. We demonstrate that the combination of pressure estimation from PIV and deformation measurement through DIC enables the precise identification of the hydrodynamic loading and structural response. The proposed methodology may help in improving our understanding of a number of fluid-structure interaction problems, such as biomimetic propulsion, aeroelasticity of airfoils, and hydrodynamic impact on marine structures.

Keywords: flow dynamics, fluid-structure interaction, pressure reconstruction, structural deformation, uncertainty

1. Introduction

In fully-coupled fluid-structure interaction (FSI) problems, forces imposed on a structure by the fluid flow causes structural deformation, which, in turn, alters the boundary conditions of the fluid, thereby modulating its dynamics. These problems are of fundamental engineering interest, as they arise in a variety of applications, such as energy harvesting [1], animal locomotion [2, 3], human speech [4], and vibration of flight structures [5]. Capturing the physics of these interactions requires detailed understanding of both the time-varying fluid loading and the dynamic response of the structure.

The fluid loading generally varies in both time and space, and thus full-field time-resolved velocity measurement is necessary to provide a thorough understanding of the interplay between the fluid and structure. Planar two-dimensional particle image velocimetry (PIV) is a ubiquitous flow measurement technique that resolves two components of a velocity field within a plane [6, 7, 8, 9, 10].

In a typical PIV experiment, the fluid is seeded with micron-sized particles that are illuminated by a laser sheet and whose motion is recorded by a camera. Two (or more) images are collected a short time apart and the velocity field is computed by cross-correlating corresponding interrogation regions within

*Corresponding author
Email address: mporfiri@nyu.edu (Maurizio Porfiri)

sequential images. Among a wide range of FSI problems, PIV has been succesfully employed to study the thrust developed by a beam vibrating in a fluid [11], a vortex impinging a deformable plate [12, 13], blood flow in a heart [14], and interaction between swimming fish and advected vortices [15].

Several methods have been devised to infer the loading on a structure given knowledge about the velocity field of the encompassing fluid. For example, the loading on flexible plates [11, 13], airfoils [16, 17], and wind turbine blades [18] has been computed from the surrounding velocity field using a control volume analysis. Alternatively, the full field pressure distribution in the flow can be reconstructed from the velocity data by relating the pressure and velocity fields through Navier-Stokes equations.

Specifically, given an experimentally measured velocity field, the unknown pressure field can be estimated either through direct integration of Navier-Stokes equations, or by taking their divergence of and solving the resulting Poisson equation for pressure [19]. The latter approach was found to be more computationally efficient [20]; however, solving the Poisson equation requires knowledge of pressure or pressure gradient information on all boundaries. In contrast, integration of the Navier-Stokes equations can produce the whole pressure field from a single reference point [19]. The accuracy of pressure reconstruction methods has been quantified through error propagation analyses [19], synthesized flow fields [21], and comparisons with theoretical and numerical solutions [22, 23, 24]. Pressure reconstruction has been employed in the study of water entry problems [25, 26], animal swimming [27, 28], vibration of soft active materials in water [29], vortex/plate interactions [30], and rotating bluff bodies [31], to name a few.

The response of solid structures to dynamic fluid loading can be evaluated from direct deformation measurements through the use of displacement sensors and/or high speed cameras. In addition to providing dynamic displacement information, digital image correlation (DIC) yields surface strain measurement in real time [32, 33, 34, 35]. Briefly, in DIC, deformation of the surface of a structure is visualized by recording the movement of a natural or applied surface speckle pattern. The two-dimensional displacement and strain fields are then computed by cross-correlating the speckle images recorded before and after deformation [33, 34], in a manner similar to PIV. Compared to alternative displacement measurement techniques, such as edge-detection via high speed cameras and point measurement via displacement sensors, DIC affords a higher level of accuracy and spatial resolution.

DIC is pervasive in experimental mechanics [34]. Precise displacement and strain measurements have been demonstrated in the analyses of strain localization in metal [36], crack growth in particulate composites [37], collapse of polymeric foams [38], failure of sandwich structures under blast loading [39, 40], delamination of composite laminates [41], stretching of soft tissues [42, 43], and compression of bone specimens [44, 45].

Deformation data have been combined with various optimization algorithms toward the identification of the external loads active on the structure [46, 47, 48, 49]. However, the load identification process is inherently an ill-posed inverse problem, and as such, small perturbations in the measurement data may result in significant errors in the load estimation [47]. Regularization methods, such as Tikhonov regularization [46], that incorporate *a priori* knowledge of the smoothness of the load have been employed to mitigate issues arising from ill-posedness [47, 48, 49, 50], but the problem remains.

The objective of this work is to demonstrate the feasibility of a combined PIV/DIC approach for determining the hydrodynamic load and structural deformation in a coupled FSI problem. To this end, we focus on a simple fluid-structure interaction problem, in which a flexible cantilevered plate bends due to a steady fluid flow perpendicular to its undeformed configuration. This archetypal setup brings forward an interesting fluid-structure interaction problem, without experimental confounds that may be associated with multiaxial structural deformations, unsteady phenomena, and free surface flows. The hydrodynamic pressure induced by the water flow on the plate elicits a structural deformation, which, in turn, imposes a change in the boundary of the fluid domain. PIV or DIC alone cannot guarantee accurate measurement of both the hydrodynamic load and the plate deformation. To mitigate this limitation, a combined PIV/DIC experimental setup is employed to capture the fluid dynamics and plate deformation under different flow conditions. The hydrodynamic drag associated with an incoming fluid flow on a rigid plate has been experimentally studied in the literature [51], thereby offering data on which we could benchmark our PIV and DIC load estimation data.

In the literature, combined measurements of the fluid dynamics and structural deformation have improved our understanding of fluid-structure interaction problems. For example, in a study on the sound production

mechanism of a saxophone mouthpiece, the velocity field of airflow in the mouthpiece was visualized by PIV and the coupled vibration of the reed was studied through raw PIV images. The analysis revealed a periodic flow velocity fluctuation in accordance with the structural vibration frequency [52]. Similarly, in a study of voice production, the flow field quantified through PIV and the structural vibration measured from high-speed imaging suggested that the rate of closure of the vocal folds is impacted by the intraglottal flow separation [53].

To date, only a few studies have examined the combination of PIV and DIC in fluid-structure interaction problems. More specifically, a combined PIV/DIC technique has facilitated the study of the aerodynamics of a flexible wing [54] and vibration and vortex shedding from an airfoil [55, 56]. In these studies, PIV acquisitions have revealed detailed velocity and vorticity morphologies in the vicinity of flexible structures, while DIC measurements allowed for refined measurement of the displacement field of the structure surface. Information gathered from these techniques were used to aid in the study of the coupling between the fluid flow and structural dynamics, but not for the estimation of the hydrodynamic loading. In fact, the hydrodynamic loading on the structure was measured only at a few fixed locations through additional load cells, without fully exploiting the potential of a combined PIV/DIC technique. In this vein, we put forward the integration of PIV and DIC toward a combined measurement of the hydrodynamic load and structural deformation.

Different from previous studies, the present work focuses on the following aspects: i) demonstrating the feasibility of a combined PIV and DIC system for full-field flow pressure estimation and structural deformation measurement; and ii) investigating the robustness of the pressure reconstruction with respect to image resolution, field of view, and interrogation window size. We opt for a simple experimental setup to assess the feasibility of a combined PIV/DIC approach and conduct a comprehensive, critical, analysis of its performance, toward laying the foundation of a robust methodology. The proposed experimental framework may facilitate future investigations of novel physical phenomena in fluid-structure interactions. Different from traditional techniques, our experimental approach allows for estimating the structural deformation and fluid loading via two independent measurement methods.

The rest of the paper is organized as follows: experimental details of the combined PIV and DIC system are presented in Sec. 2; the analysis methods are explained in Sec. 3; the results of PIV and DIC analyses along with the accuracy assessment of the current methods are presented in Sec. 4; and conclusions from our major findings are drawn in Sec. 5.

2. Experimental procedure

In this work, the deformation of an elastic plate due to a steady incoming water flow is studied using PIV and DIC; a schematic of the experimental setup is shown in Fig. 1. Specifically, a flexible plate is clamped at one end and positioned in the center of a water tunnel (Engineering Laboratory Design Inc., Lake City, MN) such that the planar surface of the plate is nominally orthogonal to the incoming flow. The clamped end of the plate is 4.8 cm below the water surface. The water tunnel test section is $0.15 \times 0.15 \times 2.4\,\mathrm{m}^3$ and can generate average flow speeds ranging from 0.5 to 20 cm/s. The depth of the water flow is $H = 11\,\mathrm{cm}$. A honeycomb flow conditioner is installed 50 cm upstream of the plate to promote a uniform velocity profile in the channel and minimize velocity fluctuations. All experiments are carried out at room temperature, for which the fluid density and viscosity are assumed to be $\rho = 1\,\mathrm{g/cm}^3$ and $\mu = 1\,\mathrm{mPa\,s}$, respectively.

Toward eliciting sufficiently large structural deformations, we use a highly compliant material, Polydimethylsiloxane (PDMS), to fabricate the plate. The flexible plates are fabricated by first mixing a SYLGARD 184 Silicone base and curing agent (Sigma-Aldrich, product number 761028) with a 10:1 ratio. The mixture is cast into a rectangular mold and left to polymerize for 2 h at 60 °C, thereby producing a 2.5 mm thick PDMS slab. The PDMS slab is then cut into strips of dimensions $40 \times 62.5 \times 2.5\,\mathrm{mm}^3$ for the experiments.

The Young's modulus of the PDMS is estimated from the fundamental vibration frequency of the plate. The detailed experimental procedure is presented in Appendix A. The effective Young's modulus is determined to be $E = 2.67\,\mathrm{MPa}$.

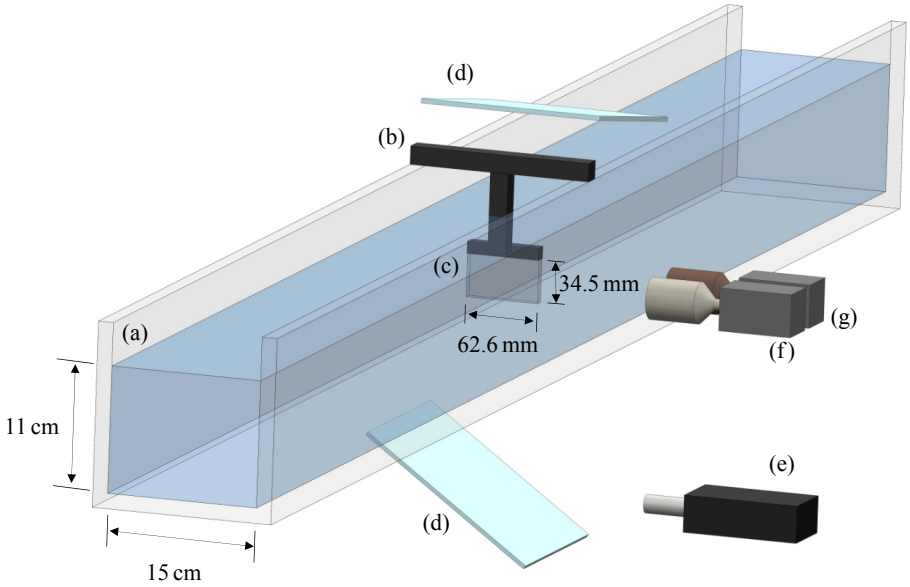

Figure 1: Schematic of the experimental setup for the combined PIV/DIC system, including: (a) water tunnel, (b) support, (c) flexible plate, (d) mirrors, (e) laser, (f) camera for PIV, and (g) camera for DIC.

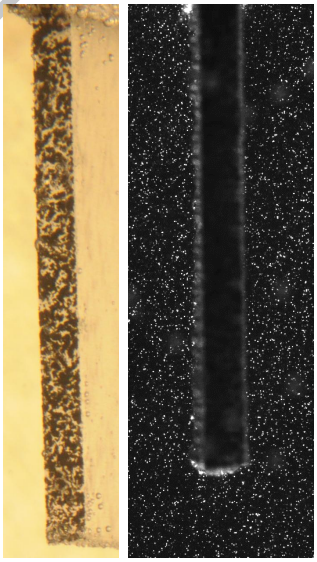

(a) (b)

Figure 2: (a) Sample image of the speckle patterns on the side of the plate recorded for DIC analysis. (b) Sample image of seeding particles recorded for PIV analysis.

Table 1: A list of experimental parameters.

Property	Symbol	Value
upstream flow speed	U	2.7–11.1 cm/s
Reynolds number	Re	935–3846
Froude number	Fr	0.034–0.139
plate length	L	34.5 mm
plate thickness	h	2.5 mm
plate span	b	62.6 mm

To record the plate deformation through DIC, a speckle pattern is created on one side of the plate. First, a thin uniform layer of a mixture of silicone base and curing agent (10:1) is applied on the side of the plate. A black toner ink powder is then sprayed onto the wet surface to generate a random speckle pattern with high contrast. The plate is heated to 60 °C for 2 h to cure the speckle pattern on the PDMS plate. The speckle pattern generated by this method is able to endure on the plate for the duration of the experiments.

During a typical DIC measurement, the speckle pattern is illuminated by a white light (GE Halogen, Flood beam, 120W, 120V). As the plate deforms, the speckle pattern is recorded by a Nikon D90 camera at a resolution of 4288×2848 pixels with a field of view of $12 \times 8\,\mathrm{cm}^2$, corresponding to $28\,\mu$m/pixel. An exemplary image of the speckle pattern is displayed in Fig. 2(a).

Polyamid particles (PSP-50, Dantec Dynamics, Skovlunde, Denmark) with a diameter of $50\,\mu$m and a density of $1.0\,\mathrm{g/cm}^3$ are used as seeding particles for the PIV study. The particle images are acquired using a Dantec PIV system (Dantec Dynamics, Skovlunde, Denmark), which comprises a 100 mJ/pulse Nd:YAG laser that generates pulses at a wavelength of 532 nm, a Phantom high speed camera, and a timer box. A light sheet is created horizontally by passing the laser beam through a series of optics, including a negative focal length cylindrical lens. The laser sheet is then reflected vertically by a mirror placed below the water tunnel through the transparent bottom of the water tunnel to intersect the plate at its mid-span. As the plate bends in the flow, seeding particles in the back of the plate may not be illuminated by the laser sheet. To resolve this issue, a second mirror is placed above and behind the plate to illuminate the back of it.

Double frame single exposure images [10] are recorded with a time delay of 1 ms between images in each image pair. The recorded images have a spatial resolution of 1200×1632 pixels with a field of view of $43 \times 58\,\mathrm{mm}^2$ (vertical $\times$ horizontal), corresponding to $36\,\mu$m/pixel. Up to 500 image pairs are recorded at 10 Hz under each flow condition for further analysis. A sample particle image is shown in Fig. 2(b).

To demonstrate the performance of the combined PIV/DIC system, we focus on a simplified problem, where both the flow and the plate deformation are steady. It has been shown that the stability of a flexible plate in a cross-flow depends on a number of factors, including the plate Reynolds number ($\mathrm{Re} = \rho U L/\mu$, where U is the upstream flow speed and L is the plate length), as well as the dimensionless bending stiffness, mass ratio between the plate and fluid, and aspect ratio of the plate [57, 58]. For the flow speeds considered in our work, the Froude number ($\mathrm{Fr} = U/(gH)^{1/2}$) ranges between 0.026 and 0.107.

In our experimental conditions, detailed in Table 1, the flow is observed to be steady and does not induce fluttering of the flexible plate. This enables DIC and PIV data to be obtained in separate experiments under the same flow condition, thereby eliminating interference of the lighting used in DIC and PIV. At a set flow speed, the speckle pattern is first recorded under white light, and particle images are subsequently acquired with laser illumination only. For a given flow condition, the plate remains at the same location in subsequent DIC and PIV images.

We comment that the current experimental design can be readily modified to address unsteady fluid-structure interaction problems. To address possible interference of the lighting for PIV and DIC, light sources with distinct emission wavelengths could be employed, and high pass and low pass filters could be installed on the cameras to enable simultaneous PIV and DIC measurements.

Table 2: Parameters varied in the load calculations through PIV pressure reconstruction and DIC inverse load identification.

	Parameter	Variation
PIV	Particle image downsampling rate	1, 2, and 3
	Interrogation window size	32×32, 8×8, and 4×4
	Integration region size	100%, 67%, and 33% of the field of view
DIC	Global load assumption	0^{th}, 1^{st}, and 2^{nd} order polynomials
	Local load regularization	0^{th}, 1^{st}, and 2^{nd} order regularizations

3. Analysis methods

3.1. DIC analysis

The speckle patterns on the plate at different flow speeds are analyzed using Ncorr [59], an open source two-dimensional DIC analysis program built in MATLAB. Ncorr incorporates a subset-based DIC algorithm in which a speckle image is partitioned into smaller regions, known as subsets, for which the deformation is calculated [59]. Our analysis is performed with a subset radius of 24 pixels to compute the two-dimensional displacement field of the plate. The deflection is evaluated as the averaged displacement in the horizontal direction at a given vertical location on the undeformed plate.

From DIC data, the hydrodynamic loading on the plate may be estimated in two possible ways. First, the distributed load on the plate could be inferred from the strain field quantified through DIC. In our experiments, the maximum bending strain at the highest value of Re is estimated to be around[1] 4×10^{-4}. However, based on results in Ref. [59], where a series of validation tests using Ncorr with a range of subset radii were conducted, strain measurements by DIC are expected to have errors from 2×10^{-4} to 1×10^{-3}. Consequently, accurate measurement of the strain field cannot be provided by DIC in the current setup, thereby hindering the application of a strain-based approach toward load reconstruction.

Alternatively, the hydrodynamic loading could be estimated from the deflection of the plate. This is the approach we undertake, based on the subpixel resolution of the the displacement field of our experimental setup [59, 60]. To this end, a finite element program is developed to estimate the load with the measured deflection as an input. Due to the ill-posed nature of the load identification problem, the form of the load needs to be assumed *a priori*. Here, we present results for two tenable approaches that incorporate either global or local assumptions on the form of the load, as summarized in Table 2. In the first approach, we assume that the load can be expressed globally as a polynomial. In the second approach, the load is assumed locally, and Tikhonov regularization is utilized for the estimation [46]. The detailed implementation of the finite element method and Tikhonov regularization is presented in Appendix B.

3.2. PIV analysis

Image pairs of the seeded flow are analyzed by PIVlab, an open source PIV analysis software programed in MATLAB [61]. Before the analysis, the plate is masked by manually locating the edges of the plate in one particle image. Due to the steady flow condition, the location of the plate remains the same in all images recorded under the same flow condition, which enables application of the same mask for all recorded images. Particle images are cross-correlated using a fast Fourier transform through a multigrid approach with decreasing interrogation window sizes from 64×64 to 32×32 pixels with a 50% overlap. A Gaussian sub-pixel interpolation scheme is used for sub-pixel resolution in the peak detection [10, 62]. Spurious vectors are removed from the vector fields. In our analysis, no more than three spurious vectors are identified from each vector field. Mean velocity fields are computed from 500 vector fields.

Small interrogation windows are required to resolve flow regions with high velocity gradients. Due to the finite particle density, when smaller interrogation windows are used in a standard PIV analysis, fewer

[1] From the maximum plate tip deflection of 1 mm observed in our experiments, the maximum strain can be estimated to be no more than 4×10^{-4}.

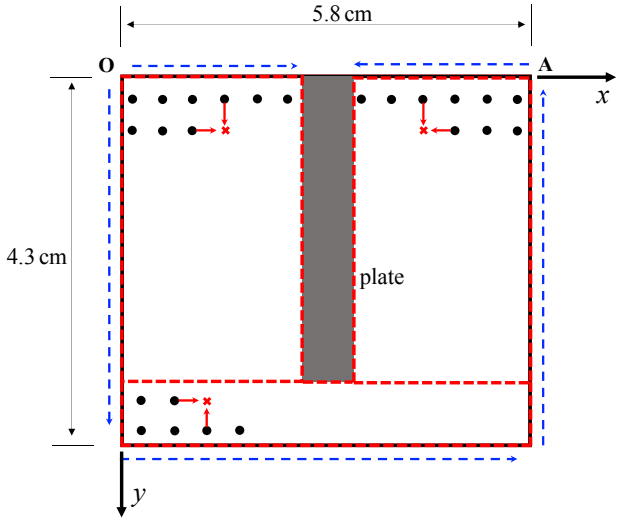

Figure 3: Schematic of the pressure integration. Blue dashed arrows indicate pressure integration directions along the boundary of the integration area, with point "O" as the starting point. Red dashed boxes represent separate integration domains, in which black dots indicate known pressure values and red crosses unknown values. The integration directions are indicated by red arrows. Point "A" represents a reference point where $p = 0$. The dimensions indicate the field of view of the camera.

particles in each window are cross-correlated and erroneous velocity vectors can be produced [63]. For a steady flow, this problem can be resolved by ensemble correlation, which has been used to produce a velocity field with high resolution [63, 64, 65]. Ensemble correlation involves computing the cross-correlation for a number of image pairs. The correlation maps are then averaged and used for peak detection and velocity calculation. Higher signal to noise ratios can be attained as more image pairs are ensemble-correlated. In this work, cross-correlation on small interrogation window sizes (for example, 8×8 and 4×4 pixels) is realized by the ensemble correlation algorithm proposed in Ref. [63].

Based on the velocity field, the pressure distribution can be reconstructed from the Navier-Stokes equations. For steady incompressible flow of a Newtonian fluid, the velocity and pressure fields are related by

$$\rho \mathbf{u} \cdot \nabla \mathbf{u} = -\nabla p + \mu \nabla^2 \mathbf{u} + \rho \mathbf{g}, \tag{1}$$

where $\mathbf{u}$ is the fluid velocity vector, p is the pressure, and $\mathbf{g}$ is the gravitational acceleration. Herein, the flow at the mid-span of the plate is assumed to be two-dimensional, such that the pressure can be constructed from the x and y velocity components only. Appendix E contains additional experiments at different cross-sections to demonstrate the secondary role of three-dimensional edge effects close to the mid-span of the plate.

The two-dimensional pressure gradient is directly calculated from Eq. (1), where the velocity gradient and Laplacian are computed by a central difference scheme. To obtain the pressure, the pressure gradient is first integrated along the boundary of the fluid domain to produce known pressure values on the boundary, as illustrated in Fig. 3. The pressure inside the domain is then integrated from the known boundary values toward the bulk of the domain. To minimize integration errors, each unknown pressure is the averaged value of line integrations from two orthogonal directions.

Due to the presence of the plate, the fluid domain is divided into three sections, as indicated by the red boxes in Fig. 3. The directions of the line integration in each section are indicated by red arrows. A reference point where $p = 0$ is chosen as the upper right corner of the integration area, as indicated by "A" in Fig. 3.

The hydrodynamic pressure on the front and back surfaces of the plate is extracted from the pressure field, and the net load on the plate is calculated as the pressure difference between both surfaces. To distinguish the hydrodynamic pressure induced by the fluid motion from the hydrostatic pressure, gravity in Eq. (1)

is neglected in the computation of the pressure distribution. The effect of viscosity on the flow pressure reconstruction in the current experiment is discussed in Appendix C. We note that in the literature, viscosity has been shown to have a secondary effect on the pressure reconstruction of high Re flows [66, 19, 67].

The uncertainty in the pressure field, ϵ_p, is estimated from the uncertainty in the velocity field and the pressure reconstruction process following the theoretical framework proposed in Ref. [19]. The uncertainty in the velocity field ϵ_u is first estimated from the cross-correlation precision, from which the uncertainty of the velocity gradients in Eq. (1) can be computed. The uncertainty in the pressure field is then derived from the integration process. Detailed computation of the uncertainty in the pressure field is presented in Appendix D.

To assess the robustness of the pressure integration approach employed in our study, we examine variations in the pressure induced by different particle image resolutions, integration area sizes, and interrogation window sizes, and compare them with the uncertainty in the pressure reconstruction. Table 2 summarizes the entire set of parametric studies we conduct in PIV.

4. Results

4.1. Combined PIV and DIC measurement

The two-dimensional plate displacement field measured by DIC in the horizontal direction (Δ_x) for an upstream flow at Re=3041 is shown in Fig. 4(a). Under the same flow condition, the velocity field around the plate is analyzed by PIV with 32×32 pixels interrogation windows and displayed in Fig. 4(b). A high velocity gradient region caused by flow separation from the free end of the plate can be noted below the plate.

From the velocity field, the reconstructed flow pressure (with the hydrostatic component removed) is presented in Fig. 4(c). The flow pressure is normalized by the dynamic pressure $p_0 = \rho U^2/2$. Corresponding to an increase of the flow speed from the clamped end to the free tip of the plate, the pressure on the front side of the plate is found to be higher at the clamped end and lower at the tip. In contrast, a wake with low velocity magnitude is created downstream of the plate, and the pressure on the back side of the plate exhibits lower values and less variation compared to the front pressure.

The pressure difference between the front and back sides of the plate, $\Delta p = p_{\text{front}} - p_{\text{back}}$, is extracted from the reconstructed hydrodynamic pressure for all Re considered. A pressure coefficient can be defined by normalizing the pressure difference as, $C_p = \Delta p/p_0$, which is shown in Fig. 5(a). The distribution of C_p on the plate at different values of Re aggregates within the uncertainty of the pressure reconstruction process, as shown by the shaded area in Fig. 5(a). The small variation of C_p under the different flow conditions is possibly a result of the limited range of Re studied in our experiments.

As an alternative way to estimate hydrodynamic loading, the plate deflection measured from DIC is utilized to compute the load on the plate. An order of magnitude estimation is obtained by assuming the load (q) to be constant, which is calculated from the plate tip deflection as $q = 8EIw(L)/L^4$, where I is the second moment of inertia of the cross-section of the plate and $w(y)$ is its deflection.

The load estimated from DIC increases quadratically as a function of U; therefore, upon normalization by the reference pressure p_0, pressure predictions from DIC at all the values of Re distribute within a narrow range (Fig. 5(a)). The load predictions from DIC are of the same order of magnitude as the pressure reconstructed from the PIV analysis. However, due to the constant load assumption, estimations from the DIC data cannot capture the pressure drop near the free end of the plate, where the mismatch between PIV and DIC becomes evident.

Using the net load on the plate, the plate deflection is predicted from the Kirchhoff-Love plate equation assuming pure cylindrical bending, which is depicted in Fig. 5(b). In comparison, the plate deflection directly measured from DIC is also displayed in Fig. 5(b). In most cases, the plate deflection predicted from PIV is smaller than the direct measurement via DIC. A maximum difference of $0.035h$ can be observed at the free end of the plate between the PIV and DIC measurement. This underestimation by PIV measurement is possibly caused by error accumulation during the indirect computation of deflections from the PIV data. It is tenable that the pressure reconstruction may be underestimated due to the finite size of the interrogation

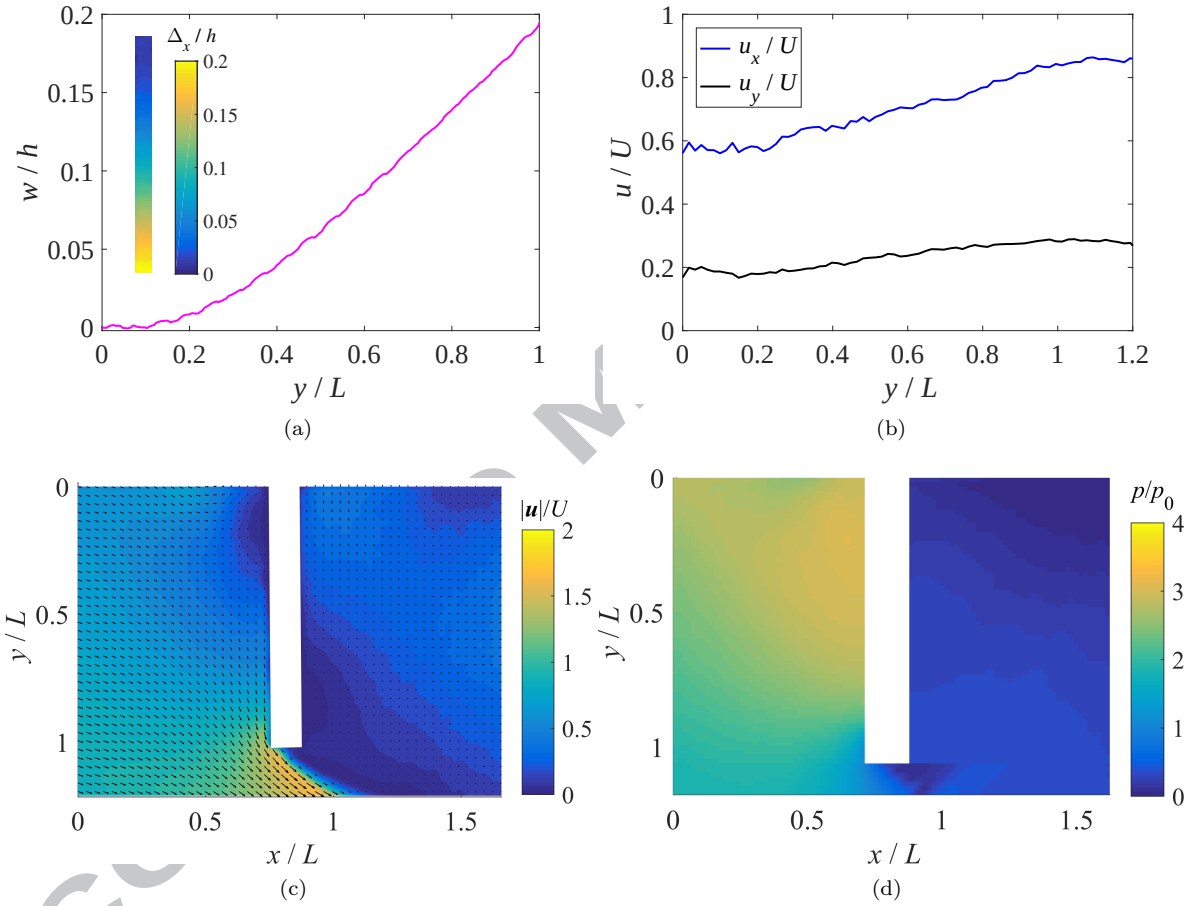

Figure 4: Measured plate displacement and flow field at Re=3041. (a) Plate deflection as a function of the vertical position. The inset shows the two-dimensional displacement field of the plate in the horizontal direction obtained from DIC analysis. (b) x and y components of the incoming flow profile as a function of the vertical position. (c) Velocity direction (arrows) and magnitude (color) around the plate produced by PIV analysis using 32×32 interrogation windows. (d) Flow pressure around the plate reconstructed from the velocity field.

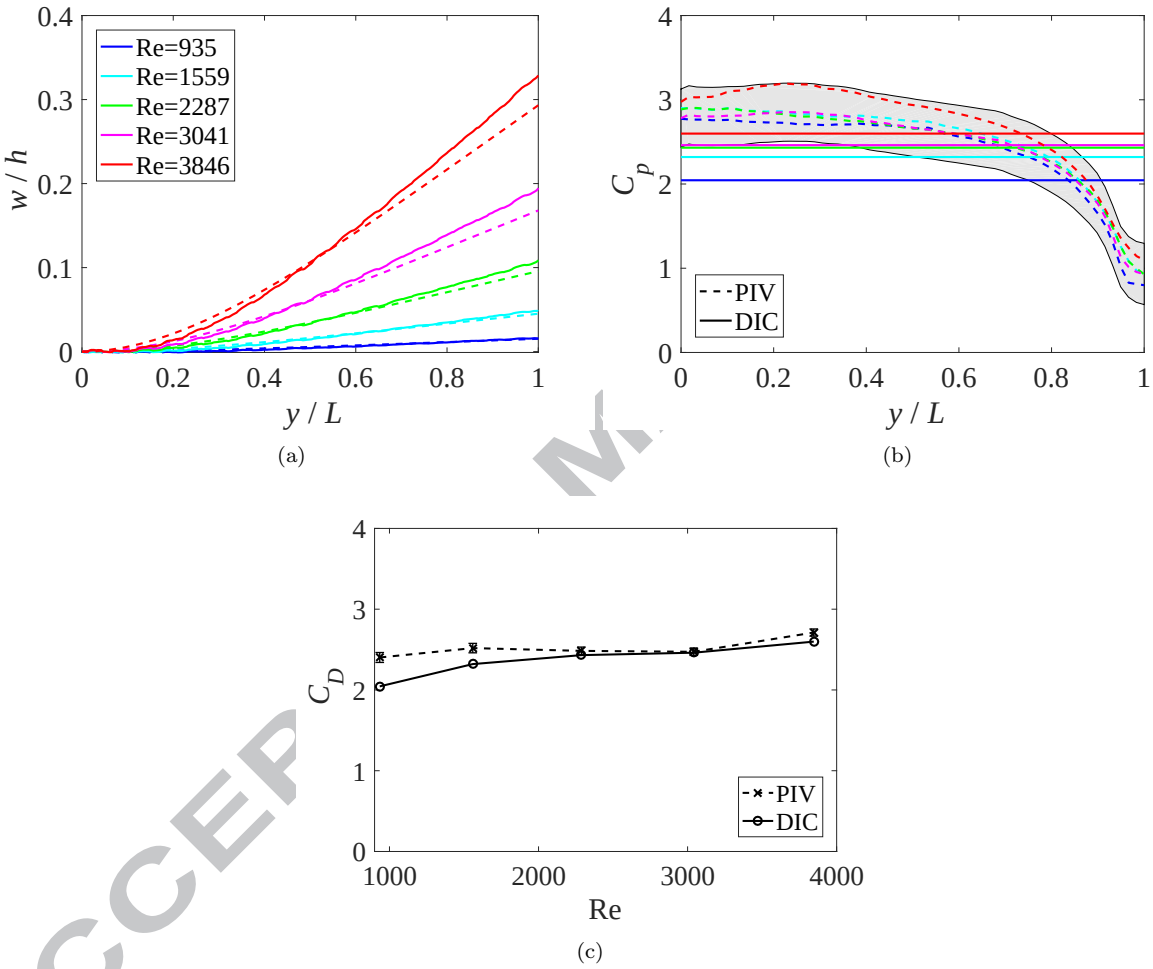

Figure 5: Comparisons of measurements from DIC and PIV experiments for plate deflection and load calculations. (a) Normalized plate deflection measured directly from DIC compared with predictions based on load calculations from PIV analysis. (b) Normalized pressure distribution on the plate reconstructed from PIV compared with predictions based on DIC measurement of the plate deflection. The shaded area represents $\pm\epsilon_{C_p}$ around the pressure reconstructed from PIV velocity data at Re=3041. (c) The drag coefficient calculated from the resultant net force on the structure estimated by PIV and DIC. Error bars represent $\pm\epsilon_{C_D}$ of the drag coefficient estimated by PIV.

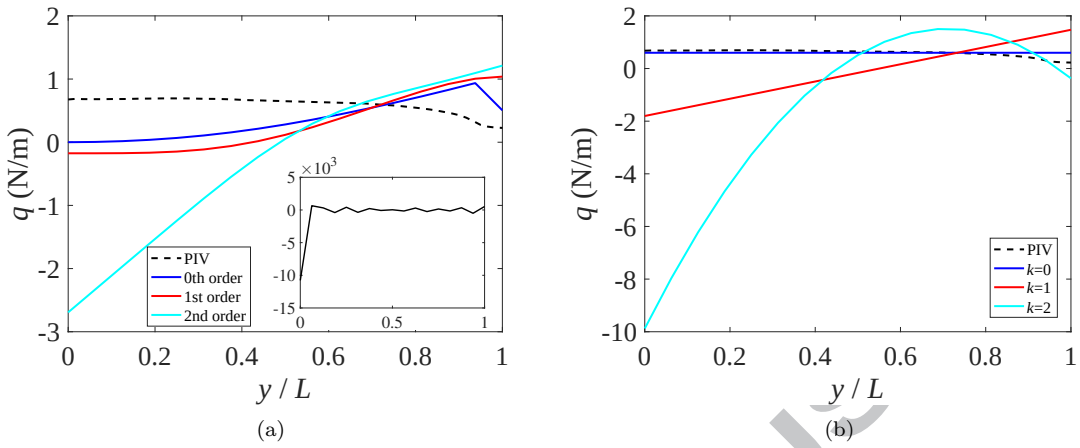

Figure 6: Inverse load calculations from the DIC measurements. (a) Local load assumptions with Tikhonov regularizations of orders 0 to 2. The inset shows the result without Tikhonov regularization. (b) Global load assumptions with polynomial of order k.

window, which might challenge the precise estimation of the velocity gradient. Especially at the free end of the plate, PIV may underestimate the velocity gradient, which could lead to a smaller value of the pressure and, ultimately, manifest into a difference between PIV and DIC results on the deflection at the free end.

We can define a drag coefficient, C_D, based on the resultant hydrodynamic force on the plate surface as

$$C_D = \frac{\int_0^L \Delta p(y) dy}{\frac{1}{2}\rho U^2 L}. \tag{2}$$

Load estimations at different values of Re from both PIV and DIC data result in nearly constant C_D with respect to Re, as shown in Fig. 5(c). The values of C_D computed from PIV and DIC exhibit a maximum difference of 0.36. Accounting for an area blockage ratio of $r = 13\%$ in the current experimental setup, the drag coefficient can be corrected by a multiplicative correction factor, $(1 - 0.5rC_D)^2$, as proposed in Ref. [66]. The resulting drag coefficient, $1.54 < C_D < 1.84$, is close to the value of $C_D = 1.98$ observed on plates in a two-dimensional flow under similar conditions [51].

In our study, we observe that three-dimensional effects induced by the edges of the plate play a secondary role, as evidenced in Appendix E. The small variations in the C_D value with Re is consistent with observations in past studies, which can be explained by the fixed flow separation point located at the free end of the plate [51]. The high and low pressure regions on the front and back sides of the plate are relatively fixed for all Re, which results in a nearly constant C_D [51].

4.2. Robustness of DIC analysis

From the deflection of the plate measured through DIC, we attempt to evaluate the hydrodynamic loading. We demonstrate two alternative approaches, in which the functional form of the hydrodynamic loading is assumed to be known at a local or global level (Table 2). Technical details on the implementation of the two approaches are summarized in Appendix B.

Figure 6(a) shows local load estimations with Tikhonov regularization of order 0 to 2, compared to load reconstructed from the PIV data. Without regularization, the estimated load is orders of magnitude different from the PIV results. With regularization, the estimated load is of the same order of magnitude as the PIV results. However, as the order of regularization increases, larger variations along the plate are observed. While these estimated loads may all produce plate deflections that are close to the measurements from DIC, the load distributions along the plate are not consistent with the flow field measured by PIV. The load near

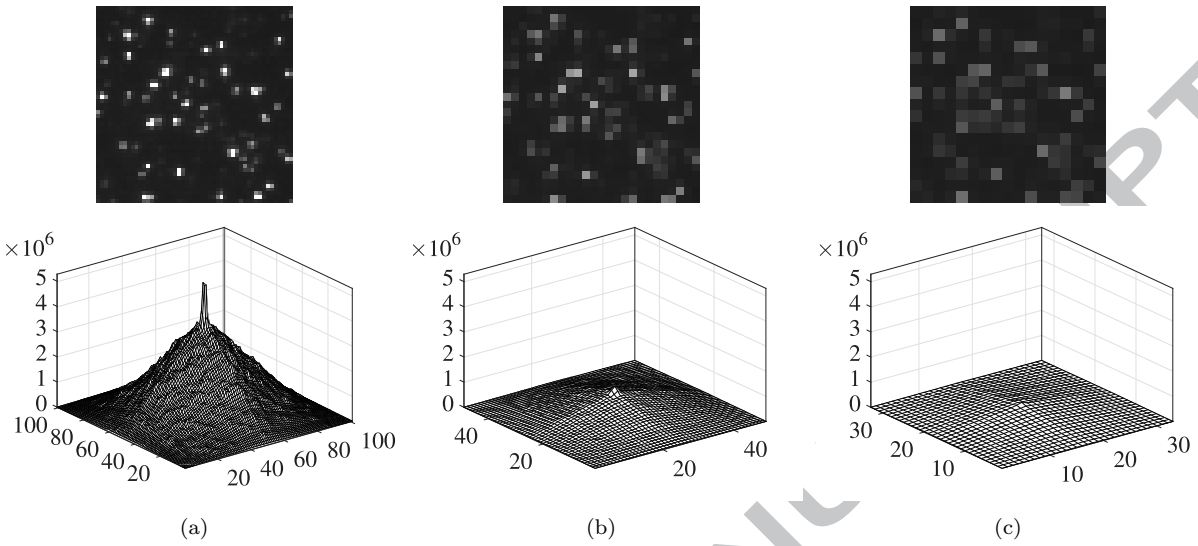

Figure 7: (a) A 50×50 pixels sample of the original particle images. Particle image in (a) downsampled with 2×2 and 3×3 averaging windows are shown in (b) and (c), respectively. The cross-correlation of each particle image with its image pair is shown on the bottom row.

the clamped end of the plate, for example, is expected to be the highest due to flow stagnation. Therefore, no reliable load estimation can be derived from DIC measurements using a local load assumption.

Globally, the load is assumed to take the form of a polynomial of degree k. The resulting load calculations with $k = 0$, 1, and 2 are displayed and compared with load reconstruction from PIV data in Fig. 6(b). We find that as k increases, load estimations from DIC measurements exhibit larger variations and deviate from the PIV reconstruction results. Similar to Fig. 6(a), the load displayed in Fig. 6(b) with $k = 1$ and 2 does not align with the expectation of a high pressure region near the clamped end of the plate. Hence, only a first order estimation of the load can be derived from the DIC data under global load assumption.

Accuracy of the load reconstruction from deflection data are affected by uncertainties in DIC measurements, which could even produce spurious rigid body motions. Such rigid body motions would challenge the representation of the elastic deflection, from which we estimate the hydrodynamic loading. Potentially, this experimental confound could be mitigated by using strain measurements from DIC as inputs for load estimations. However, the modest deformation of the plate in our experiments hinder the precise determination of the strain, as suggested by Refs. [68, 69]. Therefore, in this work, only displacement measurements from DIC have been utilized for load estimation on the plate.

4.3. Robustness of PIV analysis

The quality of two-dimensional PIV measurements is influenced by numerous sources of uncertainties [70, 23, 71, 72], which impacts the accuracy of the pressure reconstruction. In an effort to quantify the uncertainties in the pressure calculation, we explore the role of varying image resolution, size of the integration area, and velocity field resolution on the load estimation.

Poorly resolved particles may lead to low signal to noise ratio in the cross-correlation of particle images. To assess the influence of low particle image resolutions in this study, the original particle images recorded in the experiments are spatially downsampled. The downsampling is carried out by averaging the intensity of the neighboring 2×2 or 3×3 pixels of the original particle images. An example of the original and downsampled particle images and the corresponding cross-correlation values are shown in Fig. 7. A reduced signal to noise ratio can be observed in the cross-correlation as the image resolution decreases. The downsampled particle images are then used for PIV analysis and pressure reconstruction. The net load distributions on the plate at various downsampling rates are compared in Fig. 10(a).

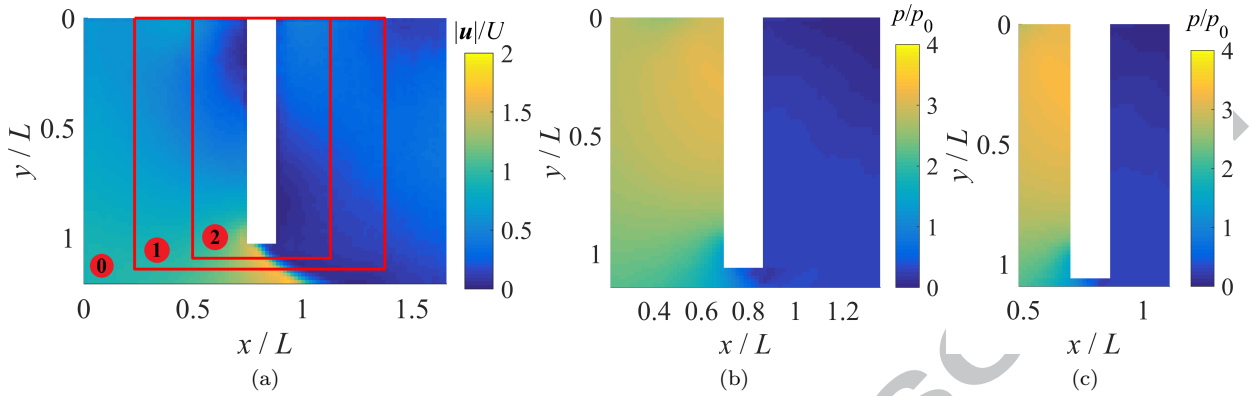

Figure 8: (a) Integration regions indicated by red boxes on the original velocity field (Re=3041) for pressure reconstruction. The reconstructed pressure distributions from region 1 and 2 are shown in (b) and (c), respectively.

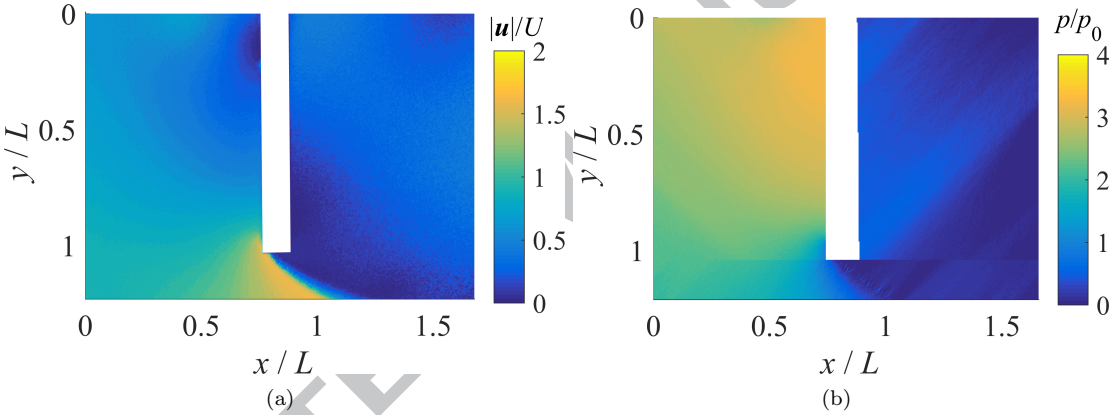

Figure 9: (a) Velocity field from ensemble correlation of 500 image pairs with 4×4 interrogation windows for Re=3041. (b) Flow pressure distribution reconstructed from the velocity field in (a).

The size of the integration area may influence the error accumulation in the process of pressure integration. To investigate this possibility, the flow pressure is reconstructed from different integration regions of the same velocity field. In addition to the pressure field reconstructed from the velocity in the whole field of view (Fig. 4(c)), we also carry out the pressure reconstruction process on two smaller integration regions, corresponding to 67% and 33% of the original integration area, as depicted in Fig. 8(a). The resulting pressure distributions are shown in Fig. 8(b) and (c). The net load on the plate extracted from the pressure distributions on three integration areas are compared in Fig. 10(b).

The high velocity gradient region below the plate is resolved at a higher resolution with smaller interrogation windows. The velocity field produced by ensemble correlation of 500 image pairs with 4×4 interrogation windows and the corresponding pressure distributions are shown in Fig. 9. Higher spatial resolution is achieved in both the velocity and pressure as smaller windows are employed. The net load on the plate reconstructed from the velocity field with different resolutions are compared in Fig. 10(c). The better resolved velocity field using 4×4 interrogation windows reveals a high pressure gradient near the tip of the plate, which is not captured by larger interrogation windows.

As evidenced in Fig. 10, when the resolution of the particle images is lowered by downsampling, the resulting pressure coefficient C_p on the plate shows a 0.24 to 0.97 deviation from the results produced by the original images. Differences in the integration area sizes result in a 0.33 variation in C_p, with the maximum difference occurring at the free end of the plate. Improved resolution of the velocity field through ensemble

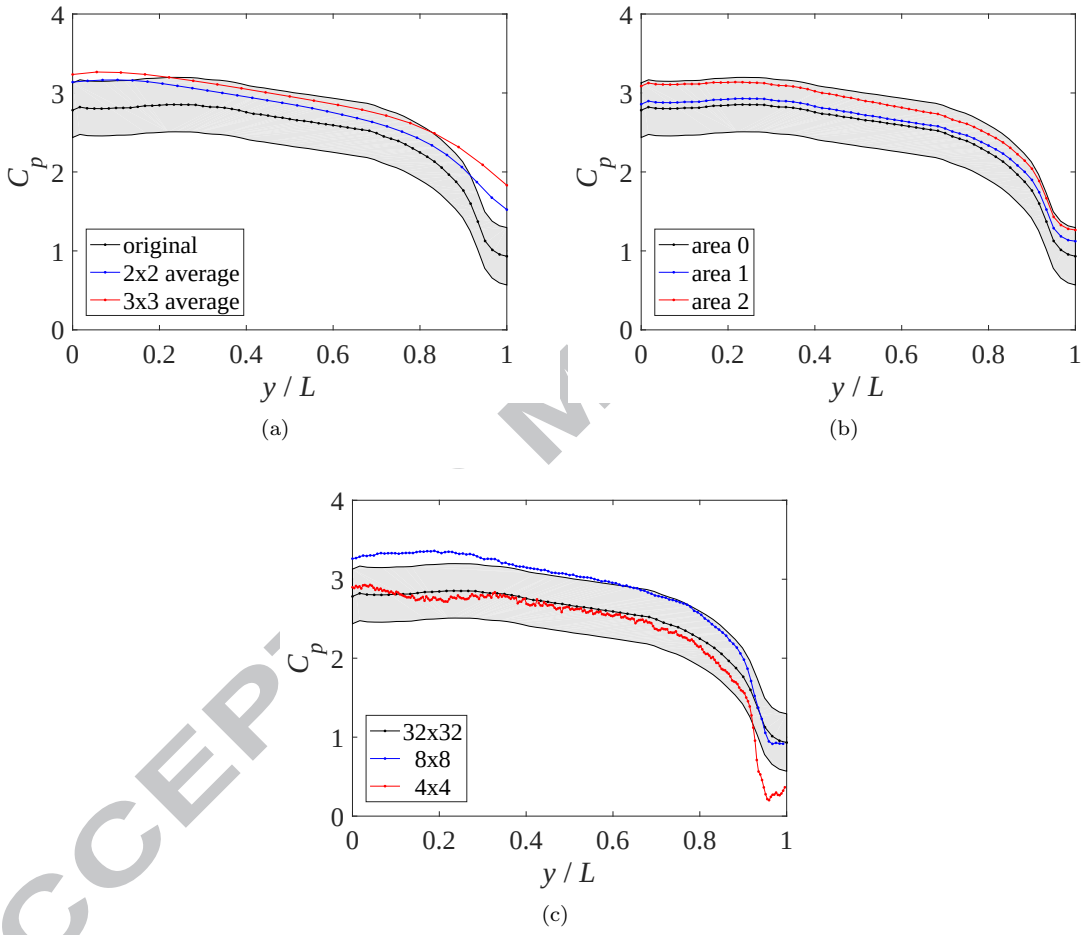

Figure 10: (a) Pressure coefficient C_p distribution reconstructed from: (a) PIV analysis of the original and downsampled particle images; (b) velocity data on the full field of view and on smaller integration areas indicated in Fig. 8(a); (c) PIV analysis using various interrogation window sizes. The shaded area represents $\pm\epsilon_{C_p}$ around the pressure reconstructed from the original velocity field processed with 32×32 windows. Re=3041 for all cases.

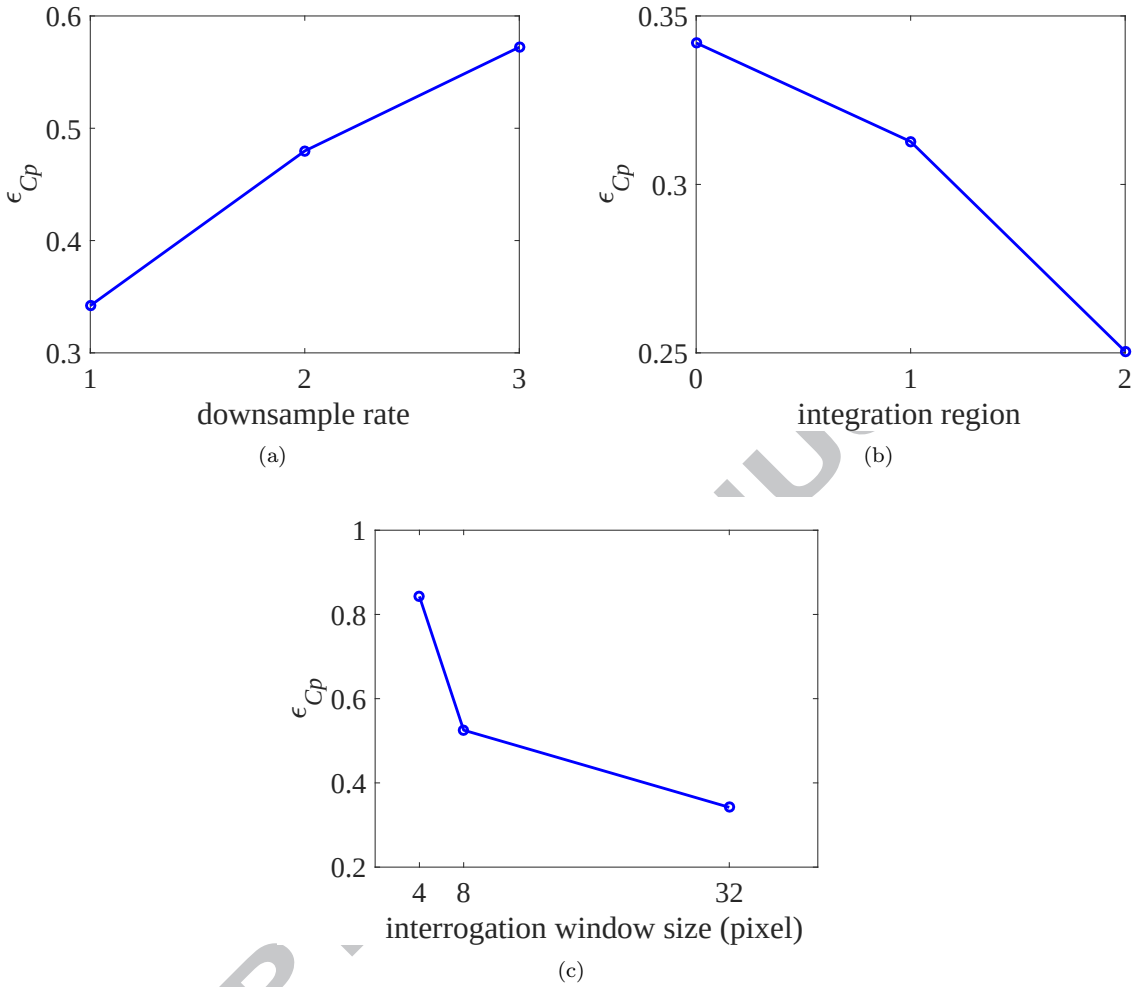

Figure 11: Uncertainty of the load estimation (ϵ_{C_p}) at the mid-point of the plate ($y/L = 0.5$) for (a) different downsample rate of the particle images, (b) different integration areas as indicated in Fig. 8(a), and (c) various interrogation window sizes. Re=3041 for all cases.

correlation exhibits less than 0.65 variation in C_p away from the free end of the plate. Since a high pressure gradient near the tip of the plate is resolved through 4×4 interrogation windows, the difference in C_p reaches 0.87.

The variations in the load calculations due to different image resolutions, integration areas and interrogation windows mostly reside within the uncertainty of the pressure reconstruction, as illustrated by the shaded area in Fig. 10. This suggests that a change in image resolutions, choices of integration regions, and interrogation windows sizes do not introduce more significant errors than the pressure reconstruction process.

These effects on the uncertainty of load calculations are further assessed and demonstrated in Fig. 11. As shown in in Fig. 11(a), the value of ϵ_{C_p} at the mid-point of the plate ($y/L = 0.5$) increases as the resolution of the particle images decreases. Similarly, pressure integration on smaller integration regions has a lower uncertainty due to error accumulation on fewer data points in the pressure integration process (Fig. 11(b)). As the interrogation window size decreases, uncertainty in the pressure coefficient increases as a result of increased uncertainty in the velocity gradient (Fig. 11(c)).

Improving the particle image resolution, shrinking the integration region around the structure, and

enlarging the interrogation window may help to achieve lower uncertainty in the load estimation. On the other hand, limited by the capability of the experimental hardware, increasing particle resolution leads to a smaller field of view of the camera. Hydrodynamic pressure reconstructed on smaller fields of view and integration regions may not contain pressure variations on a large spatial scale, which may be critical to understanding the influence of large flow patterns on the structure. In addition, larger interrogation windows cannot resolve detailed load variations on the plate. Therefore, the choices of the particle image quality, integration region and interrogation window is a balance between the desired field of view, resolution of the pressure field, and the required uncertainty level.

5. Conclusion

In this paper, we demonstrate that accurate quantification of the hydrodynamic loading and structural deformation in an FSI problem can be achieved through a combined PIV and DIC method. Using DIC, the deflection of the plate induced by the flow pressure is directly measured. The fluid flow around the plate is captured by PIV, and the reconstructed pressure field is utilized to estimate the hydrodynamic load on the plate. The fluid pressure reconstructed from PIV together with the structural displacement and strain field directly measured from DIC provide complete information of the FSI problem.

The pressure distributions at different Reynolds numbers aggregate within a small range upon normalization by the upstream dynamic pressure. Similarly, the drag coefficient C_D exhibits only small variations with respect to Reynolds number over the explored range. This is likely due to the fact that the flow separation point is always located at the free end of the plate for all experiments, as is common for sharp-edged bluff bodies of sufficiently high Reynolds number. The high and low pressure regions are confined to the front and back sides of the plate, respectively, which results in a relatively constant C_D for all Re [51].

Loading on the plate surface and plate deformation can also be indirectly estimated from DIC and PIV, respectively. DIC measurement leads to an order of magnitude estimation for the hydrodynamic loading under a constant load assumption, which shows reasonable agreement with pressure reconstruction from the flow field. Similarly, PIV offers an adequate assessment of the deflection of the plate, estimated from the integration of the plate equation using PIV-reconstructed pressure as an input.

The estimation of the load on the plate via DIC relies on the solution of an ill-posed problem, in which small errors in the measurement data may result in significant errors in the load estimation. To demonstrate the methodology, we consider two alternative approaches in which the load is reconstructed locally or globally. In the former case, the smoothness of the load is assumed locally through Tikhonov regularizations, while in the latter the load is assumed to take the form of a polynomial. Our results suggest that a global approach should be preferred, although it can only lead to an order of magnitude estimation.

The accurate reconstruction of the hydrodynamic loading should instead be undertaken through PIV. The robustness and accuracy of the pressure reconstruction from the velocity field in PIV is assessed with different particle image resolutions, areas of integration, and interrogation window sizes, which result in pressure variations that are within the uncertainty of the reconstruction process. It is evidenced that higher particle image resolution leads to lower uncertainty in the pressure reconstruction, while the size of the integration area has a minimal impact on the pressure calculation. Improved resolution of the velocity field via the use of a smaller interrogation window can result in a better resolved pressure field at the expense of an increased uncertainty. The choices of the particle image resolution, integration region, and interrogation window therefore depend on the desired field of view, resolution of the load, and the required uncertainty level.

The deformation of the plate may also be extracted from PIV data. However, the plate deflection extracted from images of the plate masking is expected to have pixel-level accuracy. In contrast, displacement measurements through DIC may afford subpixel accuracy of the order of 0.01 pixel [73, 60]. Therefore, DIC should be preferred for the measurement of plate deformation.

PIV and DIC measurements are herein conducted separately due to the secondary role of unsteady phenomena in the fluid-structure interaction. This is supported by uncertainty analysis on the drag coefficient and time resolved analysis of the plate deflection reported in Appendix F. Our analysis indicates a modest

variation in the drag coefficient, of less than 5%, and in the tip deflection of the plate, of about 2% of the total deflection.

The equipment used in this study is in line with current practice in both DIC and PIV measurement. Not only does the DIC camera provide an adequate resolution of the speckle pattern, but also the dual-pulse laser and high speed camera offer a flow resolution above one megapixel. While we have focused on a steady fluid-structure interaction problem, the state-of-the-art PIV apparatus [10] can afford measurement with high temporal resolution at reduced spatial resolution, thereby supporting real-time measurement of unsteady fluid-structure interaction problems. The interference of light sources in simultaneous PIV and DIC measurements could be avoided by implementing light sources with different wavelengths, and installing high pass and low pass filters in front of the cameras. With respect to the load estimation on the structure in an unsteady flow, a few challenges may arise in the fluid pressure reconstruction process.

First, in a high speed unsteady flow, the hydrodynamic pressure on the structure may fluctuate at high frequency due to the formation of turbulent boundary layers [74]. An accurate estimation of the time-resolved loading on the structure would require pressure reconstruction from instantaneous PIV velocity measurements with a high temporal resolution [75]. Second, due to unsteady flow condition and limited field of view, a proper reference point for the pressure may not exist in the measurement domain [76]. To address this, multiple PIV cameras could be employed to extend the field of view of the undisturbed flow domain for the accurate inference of the reference pressure.

The proposed approach could potentially be extended to three-dimensional measurements as well. In this case, one should consider the use of multiple cameras to capture the out-of-plane structural motion through three-dimensional DIC [77], and the three-dimensional velocity field reconstructed through PIV [78, 79].

The experimental design of the combined PIV/DIC system proposed in this work can be employed to study various fluid-structure interaction phenomena, including biomimetic propulsion, aeroelasticity of airfoils, and hydrodynamic impact on marine structures. The proposed system may capture and quantify both the fluid dynamic loading and structural deformation, which may help to provide a thorough understanding of the interaction between the fluid and structure.

Acknowledgements

This work was supported by the National Science Foundation under grant number CBET-1332204, and the Office of Naval Research through grant number N00014-18-1-2218 with Dr. Yapa D. S. Rajapakse as program manager. The authors thank Yasmin Abdul Manan for her help with conducting the experiments.

Appendix A. Young's modulus of the plate

In a separate experiment, the plate is clamped at one end and free on the other end, with the free end marked with a small paint dot to facilitate position tracking. The free end of the plate is initially displaced by around 10 mm and then released to vibrate freely. The free end of the plate is tracked with a high speed camera (Phantom, Dantec Dynamics, Skovlunde, Denmark) at 300 frames per second and the fundamental vibration frequency, obtained via a fast Fourier transform, is found to be $f_1 = 17.4\,\mathrm{Hz}$. The effective Young's modulus (E) of the plate is related to the fundamental vibration frequency by

$$2\pi f_1 = \frac{3.5161}{L^2}\sqrt{\frac{EI}{\rho_s bh}}, \tag{A.1}$$

where I is the second moment of inertia of the plate, while b, h, and L are the plate width, thickness, and length, respectively. The geometry of the plate is specified in Table 1. The density of PDMS is determined by measuring the volume and weight of the plate to be $\rho_s = 1.02\,\mathrm{g/cm^3}$. The effective Young's modulus calculated from Eq. (A.1) is $E = 2.67\,\mathrm{MPa}$.

Appendix B. Inverse solution of loading from displacement measurement

The steady state plate deflection (w) is related to the distributed loading (q) by the Kirchhoff-Love plate equation assuming pure cylindrical bending as [80]

$$EI\frac{d^4w(y)}{dy^4} = q(y). \tag{B.1}$$

The deflection and slope are assumed to be zero at the clamped end. Introducing a discretization by n uniform elements ($n+1$ nodes) with Hermite basis functions [81], the above equation can be converted to a linear system as

$$\mathbf{Av} = \mathbf{q}, \tag{B.2}$$

where $\mathbf{A}_{2n\times 2n}$ is the stiffness matrix; $\mathbf{v}_{2n\times 1} = [v_1, v_2, ..., v_{2n}]^T = [w_1, \theta_1, w_2, \theta_2, ..., w_n, \theta_n]^T$ contains the deflection (w_i) and slope (θ_i) of the plate at each element node, which can be directly measured; and $\mathbf{q}_{2n\times 1} = [f_1, m_1, f_2, m_2, ..., f_n, m_n]^T$ are the resultant force (f_i) and moment (m_i) at each element node, which is unknown. The boundary condition at the clamped end of the beam, $w_0 = 0$ and $\theta_0 = 0$, are already considered in Eq. (B.2). In a forward problem, the unknown system response can be solved by the known input force distribution. Here, we seek a solution for the inverse problem of the input force knowing the system response [48].

Appendix B.1. Local load assumption

If we assume a piece-wise linear distribution, $\mathbf{a}$, for the hydrodynamic load, $\mathbf{q}$ can be written as,

$$\mathbf{q} = \mathbf{Ha} \tag{B.3}$$

where $\mathbf{a}_{(n+1)\times 1}$ is a vector containing the load value at the element nodes, and $\mathbf{H}_{2n\times(n+1)}$ is the transition matrix relating the distributed load to the resultant force and momentum on the element nodes. A solution for $\mathbf{a}$ can be sought in the sense of least square approximation as

$$\mathbf{a} = (\mathbf{B}^T\mathbf{B})^{-1}\mathbf{B}^T\mathbf{v}, \tag{B.4}$$

where $\mathbf{B}_{2n\times(n+1)} = \mathbf{A}^{-1}\mathbf{H}$ is non-square and non-invertable. Tikhonov regularization [48] is employed to treat the ill-conditioned system, which leads to a solution of the problem

$$\mathbf{a} = (\mathbf{B}^T\mathbf{WB} + \gamma\mathbf{C})^{-1}(\mathbf{B}^T\mathbf{W})\mathbf{v}, \tag{B.5}$$

where $\mathbf{W}_{2n\times 2n}$ is a weight matrix on the data, which is assumed to be the identity matrix in most cases; $\mathbf{C}_{(n+1)\times(n+1)}$ is a positive definite matrix defining the order of the regularization; and γ is a positive value that describes the extent of regularization. Both $\mathbf{C}$ and γ are explicitly defined in Ref. [48]. Compared to Eq. (B.4), the new term in Eq. (B.5), $\gamma\mathbf{C}$, describes our *a priori* assumptions on the smoothness of the force vector $\mathbf{a}$.

Appendix B.2. Global load assumption

Different from the previous method where all measured deflection information is used, here we seek to derive the hydrodynamic loading based on measured deflection at selected points. First, we assume a global load distribution in the form of a polynomial of degree k,

$$q(y) = c_k y^k + c_{(k-1)}y^{(k-1)} + \cdots + c_1 y + c_0 \tag{B.6}$$

which leads to $(k+1)$ unknown load constants, $\mathbf{c}_{(k+1)\times 1} = [c_0, c_1, ..., c_k]^T$. Similar to Eq. (B.3), $\mathbf{q}$ can be related to $\mathbf{c}$ by $\mathbf{q} = \mathbf{Hc}$, with a different force transition matrix $\mathbf{H}_{2n\times(k+1)}$ relating coefficients $\mathbf{c}$ to $\mathbf{q}$. To solve for the unknown $\mathbf{c}$, $(k+1)$ measured deflection or slope values in $\mathbf{v}$ are used as known values, and all other deflection and slope values are treated as unknown.

Appendix C. Effect of viscosity on hydrodynamic pressure reconstruction

The effect of viscosity on the pressure reconstruction and load estimation is investigated here. The pressure coefficient with and without viscosity in Eq. (1) are shown in Fig. C.12 for Re=3041. Viscosity has negligible influence on the estimation of the net load on the plate surface, as evidenced in Fig. C.12. The maximum difference caused by viscous force in C_p is 0.013.

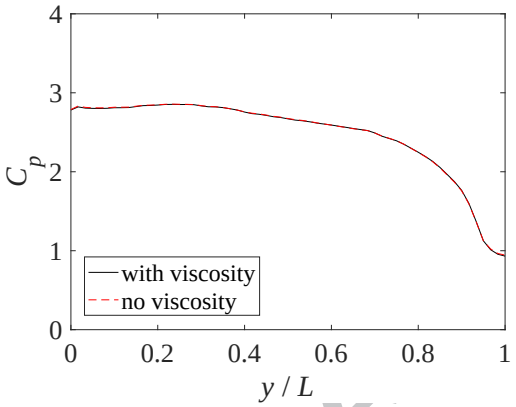

Figure C.12: Net load distribution on the plate derived from the pressure reconstruction with and without the viscosity effect.

Appendix D. Uncertainty estimation in load reconstruction

Here, we present detailed computation of the uncertainty in the pressure reconstruction from the velocity field measured through PIV. We first estimate the uncertainty in the pressure gradient from the uncertainty of each term in Eq. (1).

The uncertainty of the velocity field is estimated as

$$\epsilon_u \approx \frac{\epsilon_{\text{pix}}}{M_{\text{pix}}\Delta t}, \tag{D.1}$$

where ϵ_{pix} is the uncertainty of the cross-correlation process, which can be estimated as 0.1 pixel [19]. M_{pix} is the magnification factor of the particle images, measured as the number of pixels per unit length. Δt is the time between each pair of particle images.

The uncertainty of the convection term of Eq. (1) can be estimated from Ref. [19], as

$$\epsilon^2_{\mathbf{u}\cdot\nabla\mathbf{u}} \approx \epsilon_u^2 \left(\frac{1}{2}\frac{|\mathbf{u}|^2}{h^2} + |\nabla\mathbf{u}|^2 \right), \tag{D.2}$$

where h is the grid size of the velocity field. The uncertainty of the diffusion term can be estimated from Ref. [19], as

$$\epsilon^2_{\nabla^2 u} \approx \frac{12\epsilon_u^2}{h^4}. \tag{D.3}$$

Therefore, the uncertainty in the pressure gradient is

$$\epsilon^2_{\nabla p} = \rho^2\epsilon^2_{\mathbf{u}\cdot\nabla\mathbf{u}} + \mu^2\epsilon^2_{\nabla^2\mathbf{u}}. \tag{D.4}$$

The uncertainty in the pressure field can then be estimated from the integration of the pressure gradient.

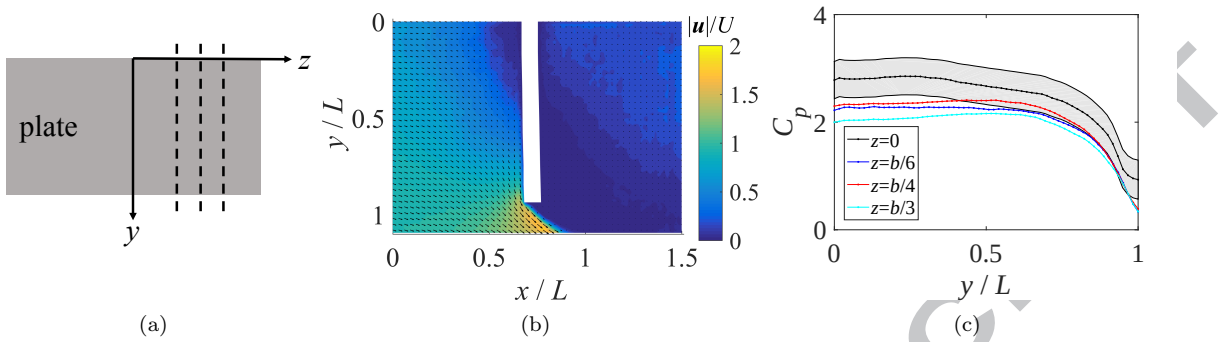

Figure E.14: (a) Definition of the z-coordinate along the span of the plate. Dashed lines show cross-sections at $z = b/6$, $b/4$, and $b/3$, where additional PIV measurements are conducted. (b) Flow field around the plate measured at the cross-section $z = b/3$ and Re = 3041, through PIV analysis with 32×32 interrogation windows. (c) Normalized pressure distribution on the plate reconstructed from PIV measured at cross-sections $z = 0$, $b/6$, $b/4$, and $b/3$ at Re = 3041. The shaded area represents ϵ_{C_p} about the pressure reconstructed from PIV velocity data at $z = 0$.

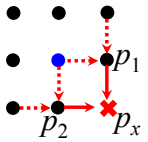

Figure D.13: Illustration of the calculation of an unknown pressure (p_x) from two neighboring grid points with known pressure values (p_1 and p_2).

The integration process of the pressure in the fluid volume is illustrated in Fig. D.13. As detailed in Sec. 3.2, an unknown pressure (p_x) at a point in the fluid domain is obtained from two neighboring points with known pressure values (p_1 and p_2) in both the vertical and horizontal directions. Specifically, the unknown pressure (p_x) in Fig. D.13 is calculated as

$$p_x = ((p_1 + h\nabla_y p_1) + (p_2 + h\nabla_x p_2))/2. \tag{D.5}$$

Note that p_1 and p_2 are not fully independent from each other. As an upper bound for the sum $(p_1 + p_2)$ in Eq. (D.5), we assume

$$\epsilon_{p_1+p_2} = \epsilon_{p_1} + \epsilon_{p_2}. \tag{D.6}$$

The uncertainty in the unknown pressure value p_x is finally

$$\epsilon^2_{p_x} = (\epsilon^2_{p_1+p_2} + h^2\epsilon^2_{\nabla_y p_1} + h^2\epsilon^2_{\nabla_x p_2})/4. \tag{D.7}$$

Equation (D.7) is used for uncertainty estimation of the entire pressure field.

Appendix E. Quantification of potential confounds from the edge effects

To quantify three-dimensional effects induced by the edges of the plate, we conduct additional PIV measurements at various cross-sections of the plate. We define a z-coordinate along the span of the plate, as shown in Fig. E.14(a). In addition to the mid-span ($z = 0$), PIV measurements are conducted on cross-sections located at $z = b/6$, $b/4$, and $b/3$.

The velocity field at $z = b/3$ is shown in Fig. E.14(b). Compared with Fig. 4(b), minimal differences in the flow field can be noted between $z = 0$ and $z = b/3$, indicating that three-dimensional effects induced by the edge of the plate have a secondary role within the span $-b/3 \leq z \leq b/3$. For completeness, the

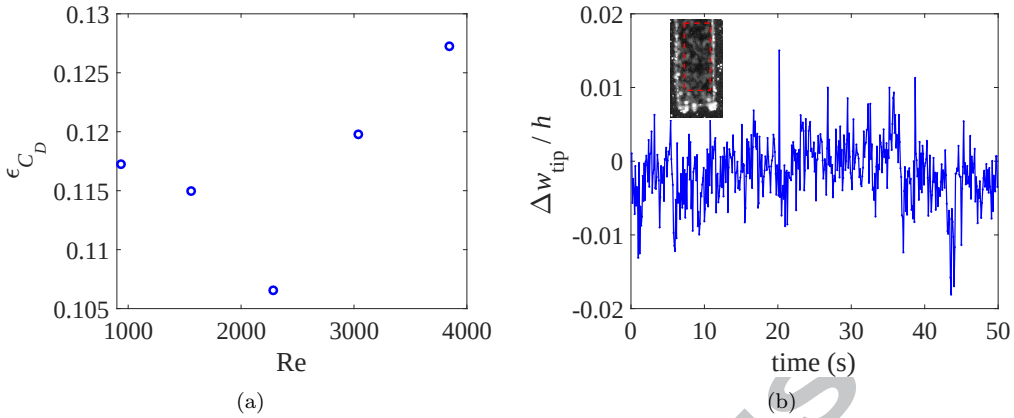

Figure F.15: (a) Uncertainty in the drag coefficient induced by the flow unsteadiness. (b) Fluttering of the plate as a function of time measured near the free end of the plate at $y/L = 0.97$ at Re = 3041. The inset shows a zoomed view of the free end of the plate on an exemplary PIV image taken with the camera focused at $z = b/3$, which preserves the speckle pattern on the side surface of the plate. The red dashed box indicates the region of interest used in temporal DIC analysis of the plate displacement. Note that the region of interest does not include the edges of the plate to avoid potential error caused by air bubbles accumulated near the edges over time.

pressure coefficient reconstructed from the velocity field at different cross-sections is displayed in Fig. E.14. The difference in C_p among all the tested cross-sections does not exceed 0.80, offering further evidence that three-dimensional effects are only secondary near the mid-span of the plate.

Appendix F. Uncertainty in load and deflection measurement due to unsteady flow

Here, we quantify the uncertainty in the hydrodynamic loading and plate deflection estimation due to unsteady flow through time-resolved measurement of the velocity field and the plate deformation.

We first estimate the uncertainty in the drag coefficient induced by the fluctuation in the velocity field. To estimate the uncertainty caused by unsteady phenomena on the pressure coefficient, the value of ϵ_u in Eq. (D.1) is assumed to be the standard deviation of the velocity field based on PIV measurement over 50 seconds (corresponding to 500 image pairs), such that $\epsilon_u = \sigma(u)$. The uncertainty in the hydrodynamic pressure is quantified following the procedure detailed in Appendix D via the current definition of ϵ_u. The uncertainties in the drag coefficients (ϵ_{C_D}) at all Re are shown in Fig. F.15(a), demonstrating a maximum relative error (ϵ_{C_D}/C_D) of less than 5%.

Due to the lack of temporal resolution in the DIC measurement, potential fluttering of the plate is estimated from the time-resolved PIV images. Although the PIV and the DIC cameras are focused on different planes during data acquisition, PIV images taken with a focal plane at $z = b/3$ preserve the speckle pattern on the surface of the plate, as shown in Fig. F.15(b). This allows for estimating the displacement of the plate in time from DIC analysis on the speckle pattern near the tip of the plate over 50 seconds (corresponding to 500 frames). Figure F.15(b) displays the tip displacement, $\Delta w_{\text{tip}}/h$, at Re = 3041. The value of $\Delta w_{\text{tip}}/h$ has a standard deviation of $\sigma(\Delta w_{\text{tip}}/h) = 4.12 \times 10^{-3}$, corresponding to 2.2% of the plate displacement measured at the same vertical location (Fig. 5(a)).

References

[1] A. Erturk, D. J. Inman, Piezoelectric Energy Harvesting, John Wiley & Sons, 2011.
[2] M. S. Triantafyllou, G. S. Triantafyllou, D. K. P. Yue, Hydrodynamics of fishlike swimming, Annual Review of Fluid Mechanics 32 (1) (2000) 33–53.
[3] J. C. Liao, A review of fish swimming mechanics and behaviour in altered flows, Philosophical Transactions of the Royal Society of London B: Biological Sciences 362 (1487) (2007) 1973–1993. doi:10.1098/rstb.2007.2082.

[4] R. Mittal, B. D. Erath, M. W. Plesniak, Fluid dynamics of human phonation and speech, Annual Review of Fluid Mechanics 45 (2013) 437–467.

[5] W. J. McCroskey, Unsteady airfoils, Annual Review of Fluid Mechanics 14 (1) (1982) 285–311.

[6] C. J. D. Pickering, N. A. Halliwell, Laser speckle photography and particle image velocimetry: photographic film noise, Applied Optics 23 (17) (1984) 2961–2969. doi:10.1364/AO.23.002961.

[7] C. J. D. Pickering, N. A. Halliwell, Particle image velocimetry: improving fringe signal-to-noise ratio with a two-step photographic process, Journal of the Optical Society of America A 2 (4) (1985) 610–615. doi:10.1364/JOSAA.2.000610.

[8] R. J. Adrian, Multi-point optical measurements of simultaneous vectors in unsteady flow – a review, International Journal of Heat and Fluid Flow 7 (2) (1986) 127 – 145. doi:http://dx.doi.org/10.1016/0142-727X(86)90062-7.

[9] R. J. Adrian, Twenty years of particle image velocimetry, Experiments in Fluids 39 (2) (2005) 159–169. doi:10.1007/s00348-005-0991-7.

[10] M. Raffel, C. E. Willert, S. Wereley, J. Kompenhans, Particle Image Velocimetry: a Practical Guide, 2nd Edition, Springer, 2007.

[11] S. D. Peterson, M. Porfiri, A. Rovardi, A particle image velocimetry study of vibrating ionic polymer metal composites in aqueous environments, IEEE/ASME Transactions on Mechatronics 14 (4) (2009) 474–483. doi:10.1109/TMECH.2009.2020979.

[12] S. D. Peterson, M. Porfiri, Energy exchange between a vortex ring and an ionic polymer metal composite, Applied Physics Letters 100 (11) (2012) 114102. doi:10.1063/1.3693184.

[13] O. Goushcha, N. Elvin, Y. Andreopoulos, Interactions of vortices with a flexible beam with applications in fluidic energy harvesting, Applied Physics Letters 104 (2) (2014) 021919.

[14] A. Kheradvar, H. Houle, G. Pedrizzetti, G. Tonti, T. Belcik, M. Ashraf, J. R. Lindner, M. Gharib, D. Sahn, Echocardiographic particle image velocimetry: A novel technique for quantification of left ventricular blood vorticity pattern, Journal of the American Society of Echocardiography 23 (1) (2010) 86 – 94. doi:https://doi.org/10.1016/j.echo.2009.09.007.

[15] J. C. Liao, D. N. Beal, G. V. Lauder, M. S. Triantafyllou, Fish exploiting vortices decrease muscle activity, Science 302 (5650) (2003) 1566–1569. doi:10.1126/science.1088295.

[16] B. W. van Oudheusden, F. Scarano, E. W. F. Casimiri, Non-intrusive load characterization of an airfoil using PIV, Experiments in Fluids 40 (6) (2006) 988–992. doi:10.1007/s00348-006-0149-2.

[17] D. Ragni, A. Ashok, B. W. van Oudheusden, F. Scarano, Surface pressure and aerodynamic loads determination of a transonic airfoil based on particle image velocimetry, Measurement Science and Technology 20 (7) (2009) 074005.

[18] C. Simao Ferreira, G. van Bussel, F. Scarano, G. van Kuik, PIV visualization of dynamic stall vawt and blade load determination, in: 46th AIAA Aerospace Sciences Meeting and Exhibit, 2008, p. 1317.

[19] B. W. van Oudheusden, PIV-based pressure measurement, Measurement Science and Technology 24 (3) (2013) 032001.

[20] Y. Murai, T. Nakada, T. Suzuki, F. Yamamoto, Particle tracking velocimetry applied to estimate the pressure field around a savonius turbine, Measurement Science and Technology 18 (8) (2007) 2491.

[21] J. McClure, S. Yarusevych, Optimization of planar PIV-based pressure estimates in laminar and turbulent wakes, Experiments in Fluids 58 (5) (2017) 62. doi:10.1007/s00348-017-2337-7.

[22] R. Panciroli, M. Porfiri, Evaluation of the pressure field on a rigid body entering a quiescent fluid through particle image velocimetry, Experiments in Fluids 54 (12) (2013) 1630. doi:10.1007/s00348-013-1630-3.

[23] A. L. Facci, R. Panciroli, S. Ubertini, M. Porfiri, Assessment of PIV-based analysis of water entry problems through synthetic numerical datasets, Journal of Fluids and Structures 55 (2015) 484 – 500. doi:http://dx.doi.org/10.1016/j.jfluidstructs.2015.03.018.

[24] A. L. Facci, M. Porfiri, S. Ubertini, Three-dimensional water entry of a solid body: A computational study, Journal of Fluids and Structures 66 (Supplement C) (2016) 36 – 53. doi:https://doi.org/10.1016/j.jfluidstructs.2016.07.015.

[25] A. Nila, S. Vanlanduit, S. Vepa, W. Van Paepegem, A PIV-based method for estimating slamming loads during water entry of rigid bodies, Measurement Science and Technology 24 (4) (2013) 045303.

[26] M. Porfiri, A. Shams, Pressure reconstruction during water impact through particle image velocimetry: Methodology overview and applications to lightweight structures, in: V. Lopresto, A. Langella, S. Abrate (Eds.), Dynamic Response and Failure of Composite Materials and Structures, Woodhead Publishing, 2017, pp. 395 – 416. doi:https://doi.org/10.1016/B978-0-08-100887-4.00013-5.

[27] J. O. Dabiri, S. Bose, B. J. Gemmell, S. P. Colin, J. H. Costello, An algorithm to estimate unsteady and quasi-steady pressure fields from velocity field measurements, Journal of Experimental Biology 217 (3) (2014) 331–336. doi:10.1242/jeb.092767.

[28] V. Mwaffo, P. Zhang, S. Romero Cruz, M. Porfiri, Zebrafish swimming in the flow: a particle image velocimetry study, PeerJ 5 (2017) e4041. doi:10.7717/peerj.4041.

[29] W. Chae, Y. Cha, S. D. Peterson, M. Porfiri, Flow measurement and thrust estimation of a vibrating ionic polymer metal composite, Smart Materials and Structures 24 (9) (2015) 095018.

[30] A. Pirnia, J. Hu, S. D. Peterson, B. D. Erath, Vortex dynamics and flow-induced vibrations arising from a vortex ring passing tangentially over a flexible plate, Journal of Applied Physics 122 (16) (2017) 164901. doi:10.1063/1.5009068.

[31] N. Fujisawa, S. Tanahashi, K. Srinivas, Evaluation of pressure field and fluid forces on a circular cylinder with and without rotational oscillation using velocity data from PIV measurement, Measurement Science and Technology 16 (4) (2005) 989.

[32] T. J. Keating, P. R. Wolf, F. L. Scarpace, An improved method of digital image correlation, Photogrammetric Engineering and Remote Sensing 41 (8).

[33] T. C. Chu, W. F. Ranson, M. A. Sutton, Applications of digital-image-correlation techniques to experimental mechanics, Experimental Mechanics 25 (3) (1985) 232–244.

[34] B. Pan, K. Qian, H. Xie, A. Asundi, Two-dimensional digital image correlation for in-plane displacement and strain

measurement: a review, Measurement Science and Technology 20 (6) (2009) 062001.
[35] M. Palanca, G. Tozzi, L. Cristofolini, The use of digital image correlation in the biomechanical area: a review, International Biomechanics 3 (1) (2016) 1–21. doi:10.1080/23335432.2015.1117395.
[36] B. Wattrisse, A. Chrysochoos, J.-M. Muracciole, M. Némoz-Gaillard, Analysis of strain localization during tensile tests by digital image correlation, Experimental Mechanics 41 (1) (2001) 29–39. doi:10.1007/BF02323101.
[37] J. Gonzalez, W. G. Knauss, Strain inhomogeneity and discontinuous crack growth in a particulate composite, Journal of the Mechanics and Physics of Solids 46 (10) (1998) 1981 – 1995. doi:http://dx.doi.org/10.1016/S0022-5096(98)00037-4.
[38] R. M. Stubbing, M. Battley, The use of digital image correlation for full field analysis of polymeric foams, in: 6th International Conference on Composites Testing and Model Identification, Aalborg, 2013, 2013.
[39] H. Arora, P. A. Hooper, J. P. Dear, Dynamic response of full-scale sandwich composite structures subject to air-blast loading, Composites Part A: Applied Science and Manufacturing 42 (11) (2011) 1651 – 1662. doi:https://doi.org/10.1016/j.compositesa.2011.07.018.
[40] N. Gardner, E. Wang, A. Shukla, Performance of functionally graded sandwich composite beams under shock wave loading, Composite Structures 94 (5) (2012) 1755 – 1770. doi:https://doi.org/10.1016/j.compstruct.2011.12.006.
[41] C. Lundsgaard-Larsen, C. Berggreen, L. A. Carlsson, Tailoring sandwich face/core interfaces for improved damage tolerance—part ii: Experiments, Applied Composite Materials 17 (6) (2010) 621–637. doi:10.1007/s10443-010-9132-4.
[42] M. A. J. Cox, N. J. B. Driessen, R. A. Boerboom, C. V. C. Bouten, F. P. T. Baaijens, Mechanical characterization of anisotropic planar biological soft tissues using finite indentation: Experimental feasibility, Journal of Biomechanics 41 (2) (2008) 422 – 429. doi:http://dx.doi.org/10.1016/j.jbiomech.2007.08.006.
[43] K. Genovese, J. D. Humphrey, Multimodal optical measurement in vitro of surface deformations and wall thickness of the pressurized aortic arch, Journal of Biomedical Optics 20 (4) (2015) 046005. doi:10.1117/1.JBO.20.4.046005.
[44] T. Hoc, L. Henry, M. Verdier, D. Aubry, L. Sedel, A. Meunier, Effect of microstructure on the mechanical properties of haversian cortical bone, Bone 38 (4) (2006) 466 – 474. doi:http://dx.doi.org/10.1016/j.bone.2005.09.017.
[45] S. P. Väänänen, S. A. Yavari, H. Weinans, A. A. Zadpoor, J. S. Jurvelin, H. Isaksson, Repeatability of digital image correlation for measurement of surface strains in composite long bones, Journal of Biomechanics 46 (11) (2013) 1928 – 1932. doi:http://dx.doi.org/10.1016/j.jbiomech.2013.05.021.
[46] A. N. Tikhonov, V. I. Arsenin, Solutions of Ill-posed Problems, New York: Wiley, 1977.
[47] O. M. Alifanov, Methods of solving ill-posed inverse problems, Journal of Engineering Physics 45 (5) (1983) 1237–1245. doi:10.1007/BF01254725.
[48] J. F. Doyle, Modern Experimental Stress Analysis: Completing the Solution of Partially Specified Problems, John Wiley & Sons, 2004.
[49] R. Adams, J. F. Doyle, Multiple force identification for complex structures, Experimental Mechanics 42 (1) (2002) 25–36. doi:10.1007/BF02411048.
[50] A.-J. Romppanen, Inverse Load Sensing Method for Line Load Determination of Beam-like Structures, Tampere University of Technology, 2008.
[51] S. F. Hoerner, Fluid-dynamic Drag: Practical Information on Aerodynamic Drag and Hydrodynamic Resistance, Hoerner, 1965.
[52] V. Lorenzoni, D. Ragni, Experimental investigation of the flow inside a saxophone mouthpiece by particle image velocimetry, The Journal of the Acoustical Society of America 131 (1) (2012) 715–721. doi:10.1121/1.3651795.
[53] S. Khosla, S. Murugappan, R. Paniello, J. Ying, E. Gutmark, Role of vortices in voice production: Normal versus asymmetric tension, The Laryngoscope 119 (1) (2009) 216–221. doi:10.1002/lary.20026.
[54] A. Timpe, Z. Zhang, J. Hubner, L. Ukeiley, Passive flow control by membrane wings for aerodynamic benefit, Experiments in Fluids 54 (3) (2013) 1471. doi:10.1007/s00348-013-1471-0.
[55] L. M. Giovannetti, J. Banks, S. W. Boyd, S. R. Turnock, Fluid structure interaction in high performance catamaran c-foils under load, in: The 5th High Performance Yacht Design Conference, 2015, pp. 171–179.
[56] L. M. Giovannetti, J. Banks, S. R. Turnock, S. W. Boyd, Uncertainty assessment of coupled digital image correlation and particle image velocimetry for fluid-structure interaction wind tunnel experiments, Journal of Fluids and Structures 68 (2017) 125 – 140. doi:http://dx.doi.org/10.1016/j.jfluidstructs.2016.09.002.
[57] A. C. Fernandes, S. M. Sefat, Flow induced fluttering and autorotation of a hinged vertical flat plate, in: ASME 2012 31st International Conference on Ocean, Offshore and Arctic Engineering, American Society of Mechanical Engineers, 2012, pp. 369–374.
[58] C. Tang, N.-S. Liu, X.-Y. Lu, Dynamics of an inverted flexible plate in a uniform flow, Physics of Fluids 27 (7) (2015) 073601. doi:10.1063/1.4923281.
[59] J. Blaber, B. Adair, A. Antoniou, Ncorr: Open-source 2d digital image correlation matlab software, Experimental Mechanics 55 (6) (2015) 1105–1122. doi:10.1007/s11340-015-0009-1.
[60] B. Pan, Z. Lu, H. Xie, Mean intensity gradient: An effective global parameter for quality assessment of the speckle patterns used in digital image correlation, Optics and Lasers in Engineering 48 (4) (2010) 469 – 477. doi:https://doi.org/10.1016/j.optlaseng.2009.08.010.
[61] W. Thielicke, E. Stamhuis, PIVlab–towards user-friendly, affordable and accurate digital particle image velocimetry in MATLAB, Journal of Open Research Software 2 (1). doi:http://doi.org/10.5334/jors.bl.
[62] L. B. Fore, Reduction of peak-locking errors produced by Gaussian sub-pixel interpolation in cross-correlation digital particle image velocimetry, Measurement Science and Technology 21 (3) (2010) 035402.
[63] C. D. Meinhart, S. T. Wereley, J. G. Santiago, A PIV algorithm for estimating time-averaged velocity fields, Journal of Fluids Engineering 122 (2) (2000) 285–289.
[64] E. Delnoij, J. Westerweel, N. G. Deen, J. A. M. Kuipers, W. P. M. van Swaaij, Ensemble correlation PIV applied

to bubble plumes rising in a bubble column, Chemical Engineering Science 54 (21) (1999) 5159 – 5171. doi:http://dx.doi.org/10.1016/S0009-2509(99)00233-X.

[65] J. Westerweel, P. F. Geelhoed, R. Lindken, Single-pixel resolution ensemble correlation for micro-PIV applications, Experiments in Fluids 37 (3) (2004) 375–384. doi:10.1007/s00348-004-0826-y.

[66] B. W. van Oudheusden, F. Scarano, E. W. M. Roosenboom, E. W. F. Casimiri, L. J. Souverein, Evaluation of integral forces and pressure fields from planar velocimetry data for incompressible and compressible flows, Experiments in Fluids 43 (2) (2007) 153–162. doi:10.1007/s00348-007-0261-y.

[67] A. Shams, S. Zhao, M. Porfiri, Hydroelastic slamming of flexible wedges: Modeling and experiments from water entry to exit, Physics of Fluids 29 (3) (2017) 037107. doi:10.1063/1.4978631.

[68] P. Zhou, K. E. Goodson, Subpixel displacement and deformation gradient measurement using digital image/speckle correlation, Optical Engineering 40 (8) (2001) 1613–1620. doi:10.1117/1.1387992.

[69] N. A. Hoult, W. A. Take, C. Lee, M. Dutton, Experimental accuracy of two dimensional strain measurements using digital image correlation, Engineering Structures 46 (Supplement C) (2013) 718 – 726. doi:https://doi.org/10.1016/j.engstruct.2012.08.018.

[70] H. Huang, D. Dabiri, M. Gharib, On errors of digital particle image velocimetry, Measurement Science and Technology 8 (12) (1997) 1427.

[71] B. H. Timmins, B. W. Wilson, B. L. Smith, P. P. Vlachos, A method for automatic estimation of instantaneous local uncertainty in particle image velocimetry measurements, Experiments in Fluids 53 (4) (2012) 1133–1147. doi:10.1007/s00348-012-1341-1.

[72] B. Wieneke, PIV uncertainty quantification from correlation statistics, Measurement Science and Technology 26 (7) (2015) 074002.

[73] Y. Q. Wang, M. A. Sutton, H. A. Bruck, H. W. Schreier, Quantitative error assessment in pattern matching: Effects of intensity pattern noise, interpolation, strain and image contrast on motion measurements, Strain 45 (2) (2009) 160–178. doi:10.1111/j.1475-1305.2008.00592.x.

[74] W. K. Blake, Turbulent boundary-layer wall-pressure fluctuations on smooth and rough walls, Journal of Fluid Mechanics 44 (4) (1970) 637660. doi:10.1017/S0022112070002069.

[75] S. Pröbsting, F. Scarano, M. Bernardini, S. Pirozzoli, On the estimation of wall pressure coherence using time-resolved tomographic PIV, Experiments in Fluids 54 (7) (2013) 1567. doi:10.1007/s00348-013-1567-6.

[76] R. De Kat, B. W. Van Oudheusden, Instantaneous planar pressure from PIV: analytic and experimental test-cases, in: Proceedings of the 15th International Symposium on Applications of Laser Techniques to Fluid Mechanics, Lisbon, Portugal, 2010.

[77] M. A. Sutton, J. H. Yan, V. Tiwari, H. W. Schreier, J. J. Orteu, The effect of out-of-plane motion on 2d and 3d digital image correlation measurements, Optics and Lasers in Engineering 46 (10) (2008) 746 – 757. doi:https://doi.org/10.1016/j.optlaseng.2008.05.005.

[78] M. Jalalisendi, S. J. Osma, M. Porfiri, Three-dimensional water entry of a solid body: A particle image velocimetry study, Journal of Fluids and Structures 59 (Supplement C) (2015) 85 – 102. doi:https://doi.org/10.1016/j.jfluidstructs.2015.08.013.

[79] M. Jalalisendi, A. Shams, R. Panciroli, M. Porfiri, Experimental reconstruction of three-dimensional hydrodynamic loading in water entry problems through particle image velocimetry, Experiments in Fluids 56 (2) (2015) 41. doi:10.1007/s00348-015-1895-9.

[80] J. M. Gere, S. P. Timoshenko, Mechanics of Materials, 4th Edition, Boston PWS Pub Co, 1997.

[81] T. J. R. Hughes, The Finite Element Method: Linear Static and Dynamic Finite Element Analysis, Dover Publications, 2000.

Highlights

- PIV and DIC are combined to estimate loading and deformation of a plate in a flow
- PIV is used to resolve the velocity field, from which pressure is reconstructed
- DIC is used to capture deformation of the plate, and loading is inversely computed
- PIV enables robust pressure measurement and accurate deformation estimation
- DIC offers precise deformation measurement and first-order identification of load